Journal of Materials Chemistry C

Accepted Manuscript

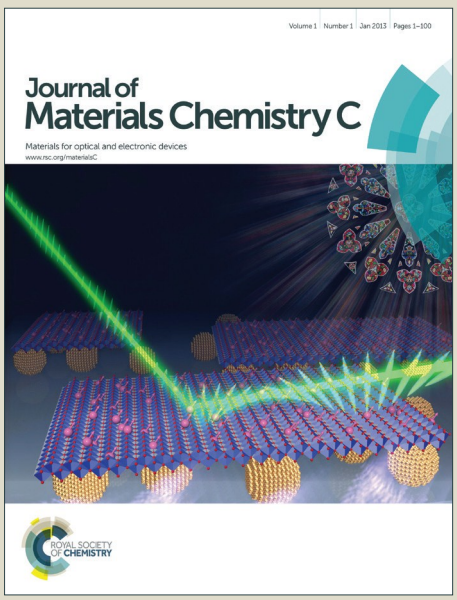

ROYAL SOCIETY OF CHEMISTRY

www.rsc.org/materialsC

Journal Name

ARTICLE

The *p*-type $Mg_2Li_xSi_{0.4}Sn_{0.6}$ thermoelectric materials synthesized by a B_2O_3 encapsulation method and using Li_2CO_3 as doping agent

Received 00th January 20xx,
Accepted 00th January 20xx

DOI: 10.1039/x0xx00000x

www.rsc.org/

Peng Gao,[a] Joshua D. Davis,[b] Viktor V. Poltavets[b] and Timothy P. Hogan*[c]

This paper presents a facile synthetic procedure for *p*-type $Mg_2(Si,Sn)$-based thermoelectric materials. The B_2O_3 flux method was used for synthesis, and Li_2CO_3 was used as the p-type doping agent. These samples showed electrical conductivities and Seebeck coefficients comparable to samples doped with pure Li, but the MgO produced during the carbonate reaction had significant influence on the lattice thermal conductivity of the materials. A peak $ZT \sim 0.7$ was obtained in the $Mg_2Li_{0.025}Si_{0.4}Sn_{0.6}$ sample.

Introduction

Thermoelectric (TE) effects refer to the generation of electricity by a temperature difference or cooling/heating created by an electric current in a material. The potential application of TE technology in waste heat recovery has recently drawn significant research interest. Generally a thermoelectric device consists of a p-type and an n-type semiconductor. The heat to electricity conversion efficiency of a thermoelectric device is determined by the dimensionless figure of merit,

$$ZT = \left(S_p - S_n\right)^2 T / \left(\sqrt{\kappa_p \rho_p} + \sqrt{\kappa_n \rho_n}\right)^2 \quad (1)$$

where S, ρ and κ are the Seebeck coefficient, electrical resistivity and thermal conductivity of the *p*-type and *n*-type semiconductors.[1] A high ZT leads to high conversion efficiency while two criteria have to be satisfied to get an optimized device performance: (1) the *p*-type and *n*-type semiconductors should have comparable transport properties and (2) both *p*-type and *n*-type have high ZT. One simple solution to meet the first criteria is to use semiconductors that could be easily doped both *p*-type and *n*-type. This may not guarantee an ideal match between the transport properties but it could eliminate potential thermal expansion mismatch between the *p*-type and *n*-type materials. The second criterion is usually satisfied by adjusting the carrier concentrations, modifying band structures and adding structures that scatter phonons stronger than charge carriers.

The $Mg_2(Si,Sn)$-based thermoelectric materials have drawn growing research interest recently due to the excellent thermoelectric property, low cost and non-toxicity of the material. The *n*-type $Mg_2(Si,Sn)$ made by substituting the Si/Sn site with Sb or Bi elements with $ZT \sim 1.2 - 1.5$ have been reported.[2-6] However, progress on the *p*-type $Mg_2(Si,Sn)$ has been slow. Generally *p*-type doping is achieved by substituting the Mg site with elements that have only one valence electron. Silver is a commonly used *p*-type dopant, but Ag-doped $Mg_2(Si,Sn)$ suffers from the low hole mobility which has limited the thermoelectric performance of the material.[7,8] A recent study has shown that alkali metals (Li, Na and K) could also be effective *p*-type dopants for $Mg_2(Si,Sn)$ materials and $ZT \sim 0.5$ has been reported for the Li-doped $Mg_2(Si,Sn)$ which is attributed to the increased hole mobility.[9] However, the handling of pure alkali metals needs extreme caution due to their high reactivity.

In this work, we present a facile chemical approach to dope $Mg_2(Si,Sn)$ using Li_2CO_3 as a doping agent instead of Li metal. Earlier studies have shown sodium acetate could be used to obtain *p*-type samples in $Mg_2(Si,Sn)$.[10,11] In our case, lithium carbonate (Li_2CO_3) was chosen instead of lithium acetate ($LiCH_3COOH$) because the carbonate has a higher lithium content and a lower price.

Experimental

1. Sample preparation

The decomposition of carbonated generates CO_2 gas and may cause pressure built-up in a sealed reaction environment. The B_2O_3 encapsulation layer could move to balance the pressure so the B_2O_3 encapsulation method is ideal for the synthesis of the carbonate-doped $Mg_2(Si,Sn)$.[12] Elemental powders of Mg (Alfa Aesar, 20 - 100 mesh, 99.8%), Si (Alfa Aesar, 100 mesh, 99.9%) and Sn (Alfa Aesar, 100 mesh, 99.85%) were mixed stoichiometrically. Different amounts of Li_2CO_3 powders were added to the $Mg_2Si_{0.4}Sn_{0.6}$ mixture to get a nominal composition of $Mg_2Li_xSi_{0.4}Sn_{0.6}$ where $0 \le x \le 0.100$. No excess

[a] Department of Chemical Engineering and Materials Science, Michigan State University, 428 S. Shaw Lane, East Lansing, Michigan, 48824, United States
[b] Department of Chemistry, Michigan State University, 578 S. Shaw Lane, East Lansing, Michigan, 48824, United States
[c] Department of Electrical and Computer Engineering, Michigan State University, 428 S. Shaw Lane, East Lansing, Michigan, 48824, United States

†Electronic Supplementary Information (ESI) available: [details of any supplementary information available should be included here]. See DOI: 10.1039/x0xx00000x

Mg was used here because excess Mg could possibly become fill the interstitial site (4b site Mg_i) and act as donors,[13] which contradicts our efforts to make a *p*-type material. The mixture was loaded to an alumina crucible (Almath Crucibles Ltd, CC22) and then covered by a layer of B_2O_3 powder (Alfa Aesar, 98.5%) in an argon-purged glovebox. A couple of graphite foils were put between the Mg-Si-Sn-Li_2CO_3 mixture and the B_2O_3 powder to minimize the inter-diffusion between the two layers. The loaded alumina crucible was then transferred from the glovebox into a box furnace in the air which was preheated to 973 K. The powder mixture was annealed at 973 K for 12 hours and an ingot was obtained after the furnace cooled from 973 K to room temperature. After the B_2O_3 layer and graphite foils were removed, the ingot (Fig. S1) was ground into ≤ 53 μm powders in the glovebox and the powders were sintered in a Pulsed Electrical Current Sintering (PECS) equipment. The PECS chamber was purged down to 10^{-3} Torr and backfilled with Ar (99.999%) to 760 Torr before the sintering process. The samples were then processed at 973 K for 15 ~ 20 minutes under a load of 30 MPa in the Ar-purged PECS chamber. The PECS-densified samples are pellets with diameter of 12.7 mm and the samples were over 95% of theoretical densities.

2. Characterization

Scanning electron microscope (SEM) images of the densified samples were taken using a JEOL 6610LV SEM equipped with an energy dispersive X-ray spectroscopy (EDX) detector. Materials cut from the pellets were ground into powder again for crystallographic phase analysis using powder X-Ray Diffraction (XRD) method. A Rigaku MiniFlex X-Ray diffractometer with a Cu $K_{\alpha 1}$ radiation source was used. Some powders were dissolved in 2 wt% HNO_3 solutions with trace amount of hydrofluoric acid (HF). The solutions were used for the compositional analysis in a Varian 710-ES axial inductively coupled plasma optical emission spectrometry (ICP-OES) instrument.

3. Transport property measurement

The room temperature densities ρ_0 (±1%) of the samples were measured using the Archimedes's principle. The thermal diffusivities D (±3%) and the heat capacities C_p (±5%) of the samples were measured directly on the pellets in a Netzsch LFA 457 instrument. The thermal conductivities were calculated as $\kappa = \rho \cdot D \cdot C_p$. The electrical conductivities σ (±7%) and Seebeck coefficients S (±7%) were measured in a ULVAC ZEM-3 instrument. Low temperature Hall mobilities and carrier concentrations were measured in a Quantum Design Versalab instrument.

Results and discussion

1. Crystallographic and compositional analysis

The powder XRD patterns of the $Mg_{2-x}Li_xSi_{0.4}Sn_{0.6}$ are shown in Fig. 1. Ideally when Si : Sn = 0.4 : 0.6, single phase solid solution would be expected and the obtained patterns showed a major phase that falls between pure Mg_2Si (#65-2988) and Mg_2Sn (#07-0274) phases.[14,15] There is no appreciable lattice constant shift as the doping level increased. This could be explained by the similar ionic radii of Mg^{2+} and Li^+ ions .[9,16,17]

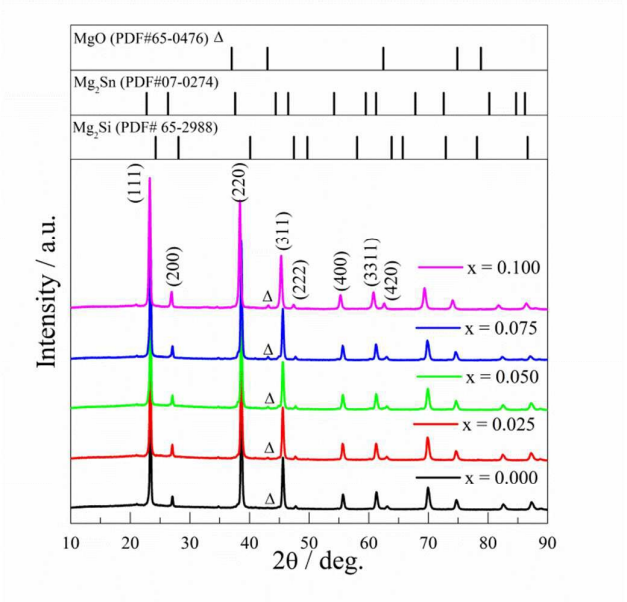

Fig. 1 Powder XRD patterns of $Mg_2Li_xSi_{0.4}Sn_{0.6}$ with different Li contents (MgO peaks were denoted by Δ)

It is also indicated in Fig.1 that the intensity of the MgO impurity peak increases as the lithium content increases. The volume fraction of MgO was estimated using a Relative Intensity Ratio (RIR) method. The RIR values of MgO (3.03) and $Mg_2Si_{0.4}Sn_{0.6}$ (7.08) were taken from the literatures.[18,19] The estimated MgO volume fractions are shown in Fig. 2. The undoped sample has the lowest MgO amount, below 1 vol%, indicating the high effectiveness of the B_2O_3 encapsulation layer in protecting samples from atmospheric oxygen. The MgO impurity concentration monotonically increases as the lithium concentration in the sample increases. All the samples were prepared under the same conditions so the surface oxidation (which might occur during PECS) was expected to be on the same level. The increased MgO level is likely to be caused by the Li_2CO_3 in the reactant as the amount of Li_2CO_3 is the only parameter that was different among all the samples. The MgO phase could also be found in the SEM images, which also shows that the MgO particle size is on micron level and the MgO phase is uniformly distributed in the sample (Fig. S2 and S3). Further discussion on the MgO formation mechanism will be presented in following sections.

The ICP-OES determined actual Li composition in each sample is also shown in Fig. 2. For all the samples the actual Li compositions are lower than the nominal composition, possibly due to the evaporation or diffusion of the lithium ion. The actual compositions show good linear correlation to the nominal compositions, indicating a consistent doping efficiency of Li_2CO_3 as the doping agent. For consistency, the nominal compositions will be used in the rest of this paper.

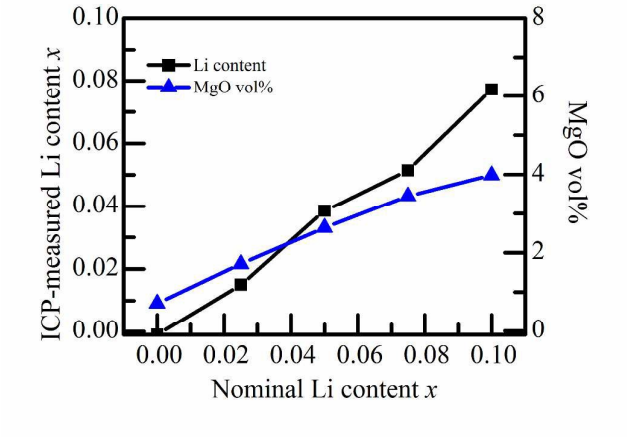

Fig. 2 The actual Li content and MgO volume fraction in the $Mg_2Li_xSi_{0.4}Sn_{0.6}$ samples

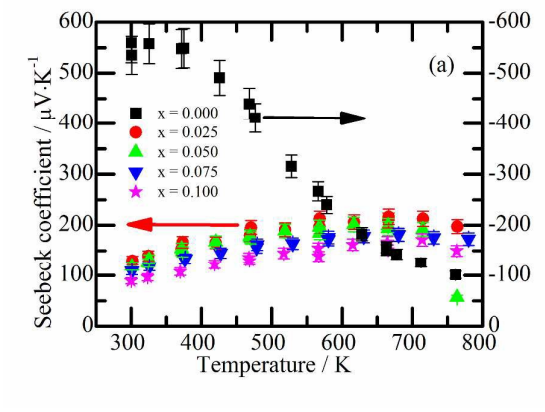

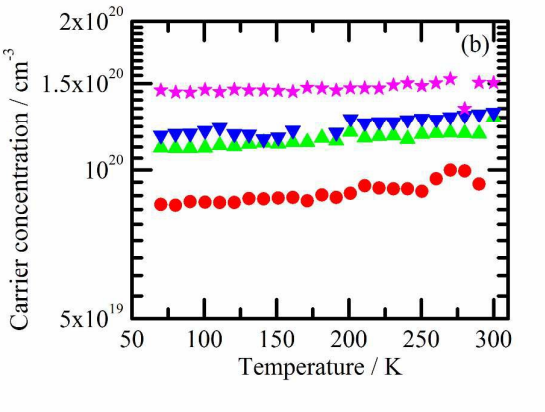

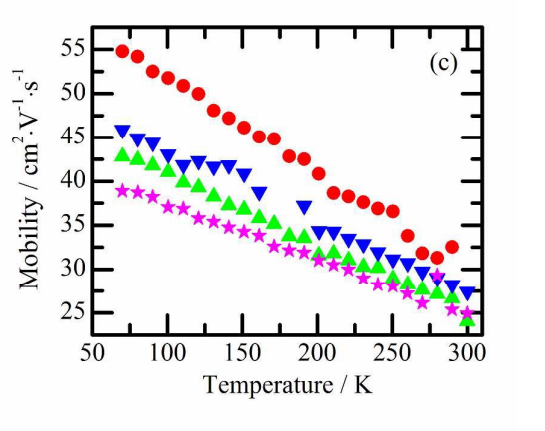

2. Transport properties

Fig. 3a shows the Seebeck coefficients of the $Mg_2Li_xSi_{0.4}Sn_{0.6}$ samples. All the doped samples have positive Seebeck coefficients while the undoped sample has negative Seebeck coefficient, indicating *p*-type semiconducting behaviour in the doped samples and *n*-type in undoped samples. This shows that Li_2CO_3 is an effective *p*-type doping agent. The undoped $Mg_2Si_{0.4}Sn_{0.6}$ displays high absolute Seebeck coefficients that decrease with increasing temperature, typical for an intrinsic semiconductor. The doped samples have lower absolute Seebeck coefficients than the undoped samples due to the increased hole concentration. The Seebeck coefficients of the doped samples increase with increasing temperature until a certain temperature at which the minority carrier activation becomes significant and the bipolar transition occurs.

The temperature dependent Hall measurements (Fig. 3b and Fig. 3c) show that the hole concentrations increase from ~ 8×10^{19} cm^{-3} to ~ 1.4×10^{20} cm^{-3} as the doping concentration increases from $x = 0.025$ to $x = 0.100$. The hole concentrations exhibit weak dependence on temperature, typical of heavily doped semiconductors. At low temperatures (~ 70 K) the least doped sample has the highest mobility of ~ 55 $cm^2/(V\cdot s)$ and the most doped sample has the lowest mobility of ~ 40 $cm^2/(V\cdot s)$. The drop in the mobility could be due to the scattering by the ionized impurities (acceptors) or the MgO impurity phase. At high temperatures (room temperature or higher), the hole mobilities tend to converge to the same value, indicating that phonon scattering was dominant for high temperature transport.

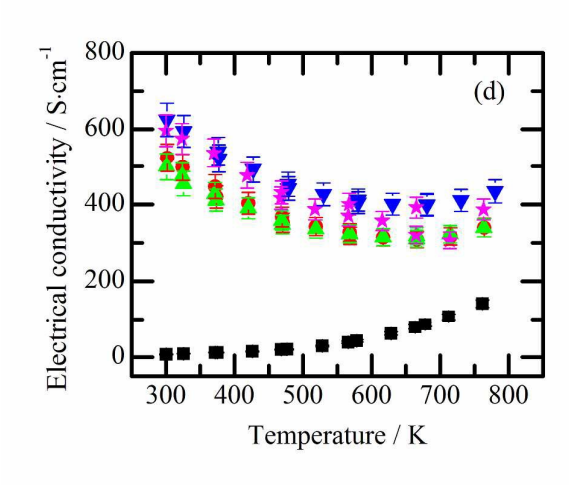

Fig. 3 Temperature dependence of the (a) Seebeck coefficients, (b) carrier concentrations, (c) carrier mobilities, (d) electrical conductivities and (e) thermal conductivities for $Mg_2Li_xSi_{0.4}Sn_{0.6}$

While the carrier concentrations are significantly increased by doping, the near room temperature mobilities for different samples are very close to each other due to the phonon-dominated scattering. As a result, the electrical conductivity of the doped sample increases as the doping concentration increases. The undoped sample has an electrical conductivity that increases with increasing temperature due to thermal activation across the bad gap. From 300 K to 600 K, the doped samples have electrical conductivities that decrease with increasing temperature due to stronger phonon scattering at high temperatures. Bipolar conduction is also observed in the electrical conductivity as the doped sample displays increasing electrical conductivities when the minority carrier activation becomes significant above 650 K.

Below 500 K the thermal conductivity of the doped samples are higher than the undoped samples. In the temperature region above 500 K the undoped sample has a higher thermal conductivity. As the total thermal conductivity consists of several contributions that responded differently to carrier concentration and temperature, a detailed analysis was performed for a better understanding of the data. The total thermal conductivities could be expressed as

$$\kappa = \kappa_l + \kappa_e + \kappa_{bp} \quad (2)$$

where κ_e , κ_l and κ_{bp} represent the electronic thermal conductivity (which is caused by hole conduction), the lattice thermal conductivity and the bipolar thermal conductivity, respectively. The κ_e could be calculated using the Wiedemann-Franz law (See ESI for calculation details)

$$\kappa_e = L \cdot \sigma \cdot T \quad (3)$$

The bipolar thermal conductivity κ_{bp} is negligible below 500 K.[6,20] Thus, the lattice thermal conductivities κ_l below 500 K could be estimated by subtracting κ_e from the total thermal conductivity.

The estimated electronic and lattice thermal conductivities are shown in Fig. 4. Samples with higher electrical conductivities show higher electronic thermal conductivities. The electronic thermal conductivities remain constant up to the bipolar transition temperature.

The more heavily doped samples have higher lattice thermal conductivities. Fig. 2 shows that the more heavily doped samples have higher MgO impurity concentrations. The increased MgO content seems to be the cause of the increased lattice thermal conductivities in doped samples. We estimated the effect of MgO impurity phase on the lattice thermal conductivity of $Mg_2Li_xSi_{0.4}Sn_{0.6}$ by treating the system as an isotropic two-phase particulate composite (Fig. 5). Our results fall between the lower and upper limit predicted by Hashin and Shtrikman and follow the same increasing trend as the MgO amount increases. (See ESI for calculation details)

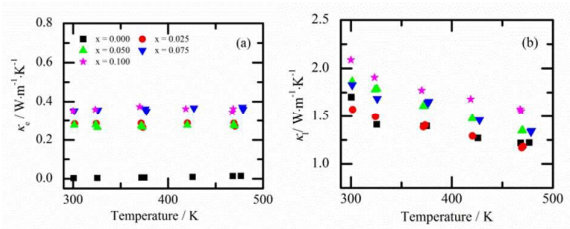

Fig. 4 The estimated (a) electronic and (b) lattice thermal conductivity for the $Mg_2Li_xSi_{0.4}Sn_{0.6}$ samples below 500 K

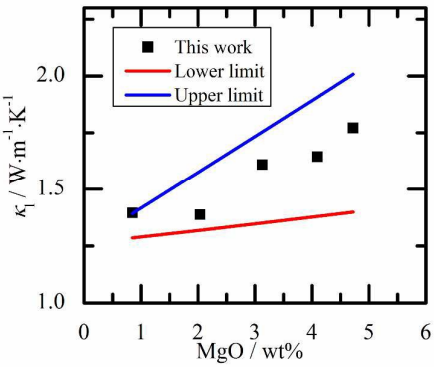

Fig. 5 Dependence of the lattice thermal conductivities for $Mg_2Li_xSi_{0.4}Sn_{0.6}$-MgO composite on the MgO weight percentage

3. Figure of merit

The dimensionless figure of merit was calculated using the measured transport data and shown in Fig. 6. All the doped samples showed appreciable enhancement in *ZT* compared with the undoped sample. Among the doped samples, the least doped sample $Mg_2Li_{0.025}Si_{0.4}Sn_{0.6}$ exhibited the highest $ZT \approx 0.7$ at 675 K.

Our results are comparable with those reported by Zhang (peak $ZT \approx 0.5$ around 750 K). The difference in the *ZT* might be caused by the difference in the Si:Sn ratio. Different Si:Sn ratio could cause a difference in the band structure and the lattice thermal conductivity, which could lead to significant difference in the transport properties and the *ZT*. Our samples have lower lattice thermal conductivities than those reported by Zhang, which is in agreement with Liu's work that $Mg_2Si_{0.4}Sn_{0.6}$ has the lowest lattice thermal conductivity in the $Mg_2(Si,Sn)$ material system.[21] Another significant difference is that Zhang's work showed a higher doping efficiency by using pure Li metal. For similar Li content levels, Zhang's samples have much higher carrier concentration than ours. This could be attributed to the different reaction/doping mechanism of using different doping agents (pure Li metal or Li_2CO_3), and it should be investigated in the future. Similar to Zhang's work, colour changes on the surface of the samples were observed in our samples (Fig. S5). Thermal cycling measurements showed no significant change in the performance for the lightly doped sample (Fig. S6 – S9). The surface changes as well as the thermal stability of those samples would be studied in the future.

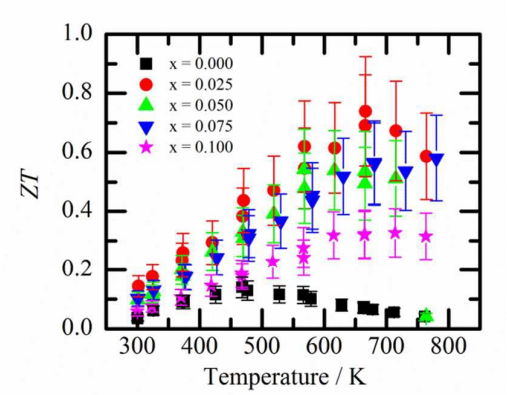

Fig. 6 The temperature dependent thermoelectric figure of merit for $Mg_2Li_xSi_{0.4}Sn_{0.6}$.

4. Discussion on the reaction and doping mechanism of Li_2CO_3

The transport data has shown that *p*-type $Mg_2Si_{0.4}Sn_{0.6}$ was successfully synthesized using Li_2CO_3 as a doping agent. The reaction and doping mechanism are not clearly revealed by the transport measurement. However, the following observations are noted.

For the reaction mechanism, replacement reaction between Li_2CO_3 and the Mg-Si-Sn mixture is not thermodynamically possible but the decomposition of Li_2CO_3 could occur.[22]

$$Li_2CO_3 \rightarrow Li_2O + CO_2 \qquad I$$

This reaction require high temperature (~ 1573 K) while our synthesis temperature was set at 973 K. Although the actual temperature of the reactant mixture might be higher due to latent heat from reaction, it is hard to determine whether or not the local temperature reached 1573 K during synthesis. It has been reported that the decomposition temperature can be lowered if CO_2 is instantly purged from the system.[23] In the synthesis environment, magnesium could react with CO_2 easily and consume the CO_2 produced by the decomposition of Li_2CO_3, making reaction I possible at lower temperatures. Overall the following reaction is proposed.

$$Li_2CO_3 + Mg \rightarrow Li_2O + MgO + CO \qquad II$$

Reaction II explains the increasing MgO content in the final product and seems to be a possible reaction routine. More experimental or theoretical evidence is needed to for better understanding of the reaction mechanism.

For the doping mechanism, the consequence of reaction II is the consumption of Mg during the reaction which could potentially create magnesium vacancies (V_{Mg}) in the material. It is well accepted that V_{Mg} act as acceptors in the $Mg_2(Si,Sn)$ materials system, so it is reasonable to raise the question whether the *p*-type behaviour in our samples were caused by Mg vacancies. To address this question, we prepared two test $Mg_2Si_{0.4}Sn_{0.6}$ samples using Na_2CO_3 and K_2CO_3 respectively as doping agent instead of Li_2CO_3. The reaction mechanism for Na_2CO_3 and K_2CO_3 are similar to reaction iii. Similar transport properties should be expected if V_{Mg} was the origin of the holes as all three different carbonates consume Mg in the same manner. However, the Na_2CO_3 and K_2CO_3 doped samples show different transport properties compared with Li_2CO_3 doped samples (Fig. S10). Meanwhile, our transport data are comparable to those reported by Zhang,[9] who used pure Li metal as a doping agent to make *p*-type $Mg_2Si_{0.3}Sn_{0.7}$ (Fig. 7). Thus, it is unlikely that the major source of holes in our samples is from magnesium vacancies.

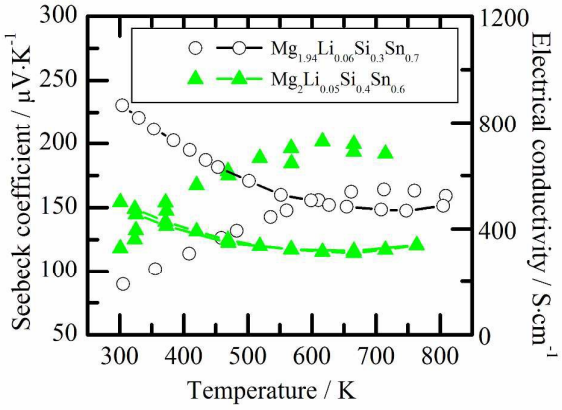

Fig. 7 Transport data of sample $Mg_{1.94}Li_{0.06}Si_{0.3}Sn_{0.7}$ with carrier concentration $n_p \approx 1.4 \times 10^{20}$ cm^{-3} reported by Zhang and sample $Mg_2Li_{0.05}Si_{0.4}Sn_{0.6}$ with $n_p \approx 1.3 \times 10^{20}$ cm^{-3} (symbols represent Seebeck coefficients and line-symbols represent electrical conductivities)

Another possible source of holes is the substitutional lithium (Li_{Mg}). The formation energies of Li_2O (466 kJ/mol) and MgO (492 kJ/mol) are very similar and the reactant mixture is a Mg-rich environment for Li_2O, it seems the following reaction could take place[22]

$$Mg + Li_2O \leftrightarrow MgO + 2Li \qquad III$$

The 'free' Li could react with the Mg-Si-Sn reactant mixture and form Li_{Mg} as proposed by Zhang, who reported Li ionization percentages below 30% for all the samples.[9] We compared the carrier concentration with the ICP-OES measured Li content and got similar "ionization" percentages (Fig. S11). Lithium is an easily activated element and our temperature dependent carrier concentration results did not show activation behaviour, either. This implies all Li_{Mg} should be fully ionized and what limits the doping efficiency seems to be the fact that not all Li become $Li_{Mg,}$ i.e. some might become interstitial Li (Li_i) on the 4b site. As discussed in the literatures, Mg_2Si/Mg_2Sn is a system that can easily accommodate Li at both the interstitial site and the Mg-substitutional site.[24-26] A pristine Mg_2Sn and a fully doped Li_2MgSn are shown in Fig. 8. However, the site preference of Li is still not clear. More theoretical research on the formation energy of Li_{Mg} and Li_i in the $Mg_2(Si,Sn)$ system is needed to better understand the point defects that could be created by Li in this system.

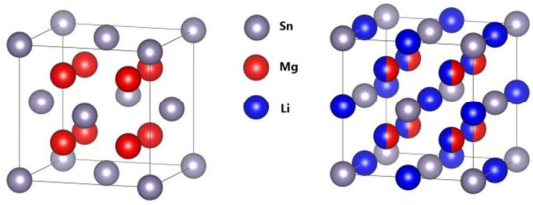

Fig. 8 Structural representations for Mg_2Sn and Li_2MgSn (Li atoms occupy both substitutional and interstitial sites in Li_2MgSn)

Conclusions

In this study, we demonstrated a facile synthetic approach that used Li_2CO_3 as the doping agent to realize *p*-type doping in $Mg_2Si_{0.4}Sn_{0.6}$ materials. The samples showed comparable transport properties compared with pure Li-doped samples reported by other groups. Meanwhile, the MgO impurity introduced during the chemical synthesis seemed to increase the lattice thermal conductivities significantly. Sample with nominal composition of $Mg_2Li_{0.025}Si_{0.4}Sn_{0.6}$ has the best peak $ZT \approx 0.7$ at 675 K. The reaction and doping mechanism needs to be investigated for further improvement in the materials performance in the future.

Acknowledgements

This material is based upon work supported as a part of the Center for Revolutionary Materials for Energy Conversion, an Energy Frontier Research Center funded by the U.S. Department of Energy, Office of Science, Basic Energy Sciences under Award Number DE-SC0001054.

Notes and references

‡ Footnotes relating to the main text should appear here. These might include comments relevant to but not central to the matter under discussion, limited experimental and spectral data, and crystallographic data.

1 D. M. Rowe, CRC Handbook of Thermoelectrics; CRC: Boca Raton, FL, 1995.
2 V. K. Zaitsev, M. I. Fedorov, E. A. Gurieva, I. S. Eremin, P. P. Konstantinov, A. Yu. Samunin and M. V. Vedernikov, *Phys. Rev. B*, 2006, **74**, 045207.
3 W. Liu, X. Tang, H. Li, K. Yin, J. Sharp, X. Zhou and C. Uher, *J. Mater. Chem.*, 2012, **22**, 13653.
4 W. Liu, X. Tan, K. Yin, H. Liu, X. Tang, J. Shi, Q. Zhang and C. Uher, *Phys. Rev. Lett.*, 2012, **108**, 166601.
5 P. Gao, I. Berkun, R. D. Schmidt, M. F. Luzenski, X. Lu, P. Bordon Sarac, E. D. Case and T. P. Hogan, *J. Electron. Mater.*, 2014, **43**, 1790.
6 P. Gao, X. Lu, I. Berkun, R. D. Schmidt, E. D. Case and T. P. Hogan, *Appl. Phys. Lett.*, 2014, **105**, 202104.
7 Y. Isoda, S. Tada, T. Nagai, H. Fujiu and Y. Shinohara, *Mater. Trans.*, 2010, **51**, 868.
8 X. Han and G. Shao, *J. Mater. Chem. C*, 2015, **3**, 530.
9 Q. Zhang, L. Cheng, W. Liu, Y. Zheng, X. Su, H. Chi, H. Liu, Y. Yan, X. Tang and C. Uher, *Phys. Chem. Chem. Phys.*, 2014, **16**, 23576.
10 S. Tada, Y. Isoda, H. Udono, H. Fujiu, S. Kumagai and Y. Shinohara, *J. Electron. Mater.*, 2014, **43**, 1580.
11 J. Tani, M. Takahashi and H. Kido, *IOP conf. series: Mater. Sci. Eng.*, 2011, **18**, 142013.
12 H. Gao, T. Zhu, X. Liu, L. Chen and X. Zhao, *J. Mater. Chem.*, 2011, **21**, 5933.
13 A. Kato, T. Yagi and N. Fukusako, *J. Phys.: Condens. Matter.*, 2009, **21**, 205801.
14 T. Zhu, Y. Cao, Q. Zhang and X. Zhao, *J. Electron. Mater.*, 2010, **39**, 1990.
15 G. S. Polymeris, N. Vlachos, A. U. Khan, E. Hatzikraniotis, Ch. B. Lioutas, A. Delimitis, E. Pavlidou, K. M. Paraskevopoulos and Th. Kyratsi, *Acta Mater.*, 2015, **83**, 285.
16 R. Shannon, *Acta Crystallogr., Sect. A: Cryst. Phys., Diffr., Theor. Gen. Crystallogr.*, 1976, **32**, 751.
17 Y. Jia, *J. Solid State Chem.*, 1991, **95**, 184.
18 E. N. Nikitin, E. N. Tkalenko, V. K. Zaitsev, A. I. Zaslavskii and A. K. Kuznetsov, *Izv. Akad. Nauk. SSSR, Neorg. Mater.*, 1968, **4**, 1902.
19 K. Hirata, K. Moriya and Y. Waseda, *J. Mater. Sci.*, 1977, **12**, 838.
20 J. Bahk, Z. Bian and A. Shakouri, *Phys. Rev. B*, 2014, **89**, 075204.
21 W. Liu, X. Tan, K. Yin, H. Liu, X. Tang, J. Shi, Q. Zhang and C. Uher, Phys. Rev. Lett., 2012, **108**, 166601.
22 I. Barin, *Thermochemical Data of Pure Substances*, VCH, Berlin, 1995. part VII, pp. 809, 972, 1001 and 1014.
23 A. N. Timoshevskii, M. G. Ktalkherman, V. A. Emel'kin,B. A. Pozdnyakov and A. P. Zamyatin, *High Temp+*, 2008, **46**, 414.
24 T. Moriga, K. Watanabe, D. Tsuji, S. Massaki and I. Nakabayashi, *J. Solid State Chem.*, 2000, 153, 386.
25 D. Larcher, A. S. Prakash, J. Saint, M. Morcrette and J. Tarascon, *Chem. Mater.*, 2004, **16**, 5502.
26 H. Kim, J. Choi, H. Sohn and T. Kang, *J. Electrochem. Soc.*, 1999, **146**, 4401.
27 …

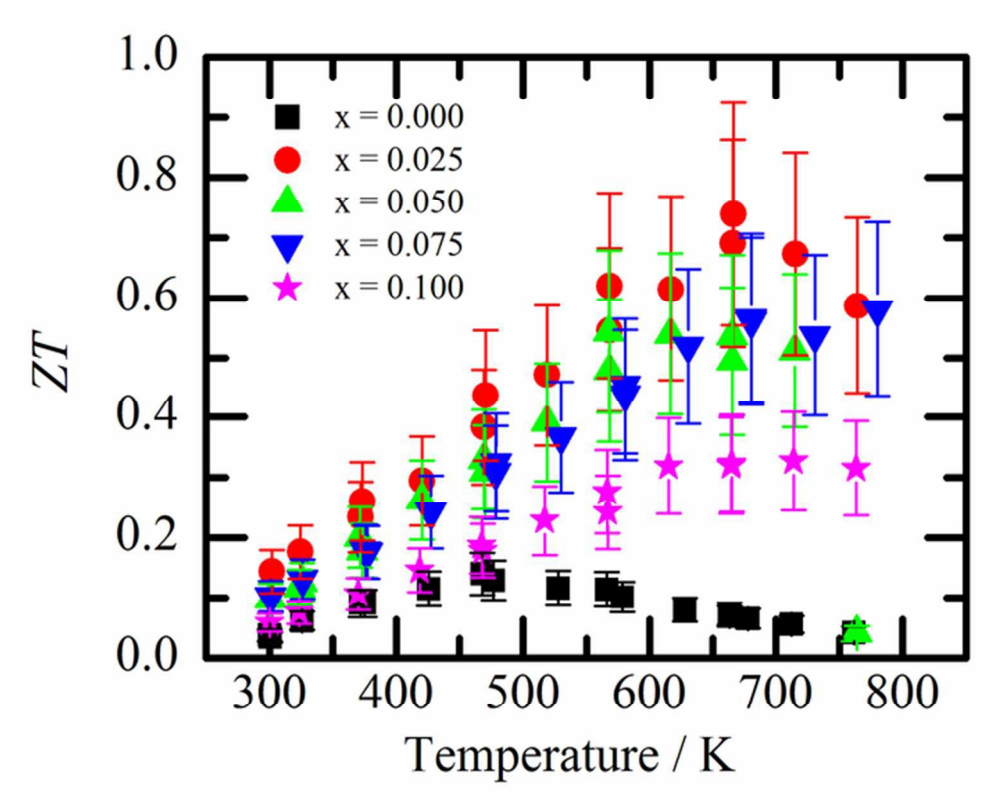

60x49mm (300 x 300 DPI)

The *p*-type $Mg_2Li_xSi_{0.4}Sn_{0.6}$ were synthesized by a B_2O_3-encapsulation method using Li_2CO_3 as doping agent and showed significant improvement in *ZT*